

# Circumstellar environments – V. The asymmetric chromosphere and dust shell of $\alpha$ Orionis

C. J. Skinner,<sup>1\*</sup> S. M. Dougherty,<sup>2,3†</sup> M. Meixner,<sup>4</sup> M. F. Bode,<sup>3</sup> R. J. Davis,<sup>5</sup>  
S. A. Drake,<sup>6</sup> J. F. Arens<sup>7</sup> and J. G. Jernigan<sup>7</sup>

<sup>1</sup>*Institute of Geophysics & Planetary Physics, Lawrence Livermore National Laboratory, PO Box 808, Livermore, CA 94551–9900, USA*

<sup>2</sup>*Physics & Astronomy, University of Calgary, University Drive N.W., Calgary, Alta, Canada T2N 1N4*

<sup>3</sup>*Astrophysics Group, School of Engineering, Electronics & Physics, Liverpool John Moores University, Byrom Street, Liverpool L3 3AF*

<sup>4</sup>*Astronomy Department, MC 221, 1002 W. Green Street, University of Illinois, Urbana, IL 61801, USA*

<sup>5</sup>*Nuffield Radio Astronomy Laboratories, Jodrell Bank, Macclesfield, Cheshire SK11 9DL*

<sup>6</sup>*NASA Goddard Space Flight Center, Code 668-(HEASARC), Greenbelt, MD 20771, USA*

<sup>7</sup>*Space Sciences Laboratory, University of California, Berkeley, CA 94720, USA*

Accepted 1997 January 2. Received 1996 December 30; in original form 1996 June 26

## ABSTRACT

We report new mid-infrared and radio images of the M supergiant  $\alpha$  Orionis. The radio images, taken with MERLIN<sup>1</sup> and the Very Large Array, resolve the chromosphere of the star at a wavelength of 6 cm, showing that the radio-emitting region has between two and three times the diameter of the optical photosphere. The infrared images, taken at the UK Infrared Telescope (UKIRT) using the Berkeley Infrared Camera, show that the dust shell is resolved. Images taken one year apart show great changes in morphology, which suggests that the dust shell is being asymmetrically illuminated by a stellar radiation field that is strongly affected by the presence and evolution of spots on the stellar surface. We present a new model of the circumstellar environment of the star, which fits the infrared and radio images and the spectral energy distribution (SED), and is consistent with recently reported *Hubble Space Telescope* observations. The chromospheric structure is determined quantitatively and the inner dust shell structure qualitatively with this model. We find that the inner radius of the dust shell is approximately 0.5 arcsec, which disagrees with a number of interferometric measurements that have resulted in an inner radius close to 1.0 arcsec. We are unable to explain this difference.

**Key words:** stars: chromospheres – circumstellar matter – stars: individual:  $\alpha$  Ori – supergiants – infrared: stars.

## 1 INTRODUCTION

Fairly massive stars (those within initial masses  $\approx 10$ – $30 M_{\odot}$ ) are expected to experience a phase (or phases) during their post-main-sequence evolution when they swell to enormous size and develop very low effective temperature. During this M supergiant phase, they can

\*Present address: Space Telescope Science Institute, 3700 San Martin Drive, Baltimore, MD 21218, USA; on assignment from the Space Sciences Department of the European Space Agency.

†Present address: Dominion Radio Astrophysical Observatory, PO Box 248, White Lake Road, Penticton, BC, Canada V2A 6K3.

<sup>1</sup>MERLIN: the Multi-Element Radio Linked Interferometer Network, a national facility operated by the University of Manchester on behalf of PPARC.

experience significant mass loss: in a survey of these stars using *IRAS* data, Skinner & Whitmore (1988) determined mass-loss rates in the range  $10^{-7}$  to more than  $10^{-4} M_{\odot} \text{ yr}^{-1}$ . During extensive periods as an M supergiant, a massive star could thus lose a significant fraction of its initial mass, strongly influencing its subsequent evolution.

However, despite their importance in stellar evolution, M supergiants are in general not very well understood. They are believed to possess massive stellar winds, but the wind properties are in most cases difficult to determine, and no comprehensive multiwavelength, multisource study specifically of the winds has ever been made. By and large the wind speeds are thought to be low ( $\approx 10$ – $20 \text{ km s}^{-1}$ ), and this implies that high spectral resolution is needed to determine the speed. Because M supergiants are very red,

they are typically not very bright visually, and because the winds are very cool ( $T \leq 1000$  K) there are relatively few spectral lines that can be used as wind diagnostics that are not confused by interstellar or photospheric lines. Therefore wind speeds have been measured for only a few M supergiants. Similarly, mass-loss rates have not easily been determined. In their much less luminous and lower mass counterparts the asymptotic giant branch (AGB) stars, gas mass-loss rates can often be measured to reasonable accuracy by modelling the rotational lines of CO observed in the mm and submm wavelength regions (e.g. Knapp & Morris 1985). In the case of the M supergiants, however, CO rotational lines have been distinguished by their non-detection or faintness. Dust grains condense in the cool winds of many of the M supergiants, leading to infrared (IR) excesses which can in some cases be very large. These excesses can be used to determine the mass of dust in the wind, which can then be converted to a total mass-loss rate using a number of assumptions (e.g. Rowan-Robinson et al. 1986; Skinner & Whitmore 1988; Sylvester, Barlow & Skinner 1994). The major uncertainties in these latter techniques are the gas-to-dust ratio and the wind speed, neither of which is known in most cases.

The best studied of the M supergiants is  $\alpha$  Orionis, or Betelgeuse, because it is relatively nearby ( $\approx 200$  pc), visually very bright ( $V \approx 0$ ), and has an appreciable mass-loss rate measured via CO rotational emission (e.g. Knapp & Morris 1985), 21-cm H I emission (Bowers & Knapp 1987), various optical lines in the wind (e.g. Maun & Querci 1990) and dust emission (e.g. Rowan-Robinson et al. 1986; Skinner & Whitmore 1987; Danchi et al. 1994). Since it is large and nearby,  $\alpha$  Ori is also frequently a subject of attempts to measure stellar diameters. Non-redundant masking observations of  $\alpha$  Ori by Wilson et al. (1992) showed the presence of hotspots on the surface of the star. These spots were observed to evolve on a time-scale of a year or less, consistent with a theoretical prediction by Schwarzschild (1975). Speckle images by Hebden, Eckart & Hege (1987) revealed the presence of an H $\alpha$ -emitting chromosphere more than twice the size of the photosphere. This confirmed the conclusions of a number of radio studies of  $\alpha$  Ori (e.g. Newell & Hjellming 1982) which had revealed a free-free continuum thought to be indicative of a chromosphere or partially ionized wind.

Models of the circumstellar environment of  $\alpha$  Ori by a number of different groups have resulted in somewhat different conclusions. Skinner & Whitmore (1987, hereafter SW87) concluded that the dust-to-gas ratio was much lower for  $\alpha$  Ori than for the interstellar medium (ISM) (0.007) or for typical oxygen-rich AGB star outflows (0.006, Knapp 1985). They also concluded that an extended chromosphere was needed to explain both the slope of the IR excess and the large radio excess. On the other hand, Rowan-Robinson et al. (1986) and Danchi et al. (1994) concluded that the inner radius of the dust shell was much larger than assumed by SW87 (who based their inner radius on the expected condensation temperature of silicate dust grains in radiative equilibrium with the stellar photospheric radiation field). However, they ignored any effects of a chromosphere. Spatial interferometry of the  $\alpha$  Ori dust shell has implied that the inner radius of the dust shell lies at a distance from the star where the dust temperature is only 200–400 K (e.g.

Danchi et al. 1994), whereas direct imaging has suggested a smaller dust-shell inner radius (e.g. Bloemhof, Townes & Vanderwyck 1984; Danchi et al. 1992), corresponding to a dust temperature closer to 700 K.

In this paper we report direct images of the dust shell around  $\alpha$  Ori in the mid-IR, and radio interferometer observations of the chromosphere. In Section 2 we present the radio observations, and in Section 3 the mid-IR images. In Section 4 we describe a new model for  $\alpha$  Ori taking all these new data into account, and in Section 5 we discuss the implications of the results.

## 2 RADIO OBSERVATIONS

### 2.1 MERLIN observations

Observations at 5 GHz (6 cm) of  $\alpha$  Ori were obtained using the Nuffield Radio Astronomy Laboratory MERLIN interferometer array on 1992 December 4. Our intermediate frequency (IF) of bandwidth 15 MHz was used, centred on a frequency of 5.000 GHz. The longest baseline is 215 km (3.6 M $\lambda$  at 5 GHz), giving a nominal resolution of 40 mas. The total integration time for the observation of  $\alpha$  Ori was approximately 600 min. The data were taken using a phase referencing method in which 180-s observations of  $\alpha$  Ori were interleaved with 45-s observations of the nearby bright phase reference source 0550 + 032 (B1950). The absolute flux density scale was established by an observation of 3C 286, whose flux density was assumed to be 7.309 Jy at 5 GHz. This gave a flux of  $0.587 \pm 0.025$  Jy for 0550 + 032.

The data were initially edited and amplitude calibrated using MERLIN data reduction software. Phase calibration and mapping was then carried out with the Astronomical Image Processing System (AIPS) software of the National Radio Astronomy Observatory.<sup>2</sup> The visibilities of the phase reference source were calibrated using the self-calibration method and the resulting complex antenna gain solutions were interpolated and applied to the  $\alpha$  Ori data.

### 2.2 VLA observations

The 5-GHz VLA observation was obtained on 1990 April 28 using the VLA in its highest resolution (A) configuration (with a maximum baseline of 36 km, or 0.6 M $\lambda$  at 5 GHz), giving a resolution of 340 mas. Two IFs (4.8851 and 4.8351 GHz), each of bandwidth 50 MHz, were used for the 20-min observation. Similar to the MERLIN observations, the complex gains of the 26 antenna array were monitored by frequent observations of 0529 + 075 (B1950). The absolute flux calibration was established by an observation of 3C 48, where we assumed a flux of 5.608 Jy (IF1) and 5.662 Jy (IF2). This gave a flux for 0529 + 075 of  $1.737 \pm 0.010$  Jy (IF1) and  $1.740 \pm 0.009$  Jy (IF2). Phase calibration of the antenna gains was then achieved by assuming 0550 + 032 to be a point source, and applying the derived antenna gains to the observation of  $\alpha$  Ori.

<sup>2</sup>The NRAO is operated by Associated Universities, Inc., under contract with the US National Science Foundation.

### 2.3 Radio data analysis

The calibrated visibilities were Fourier transformed and the resulting images CLEANED to produce the final synthesized images, shown in Figs 1 and 2. Two-dimensional (2D) Gaussian fits to the emission in these images suggest that

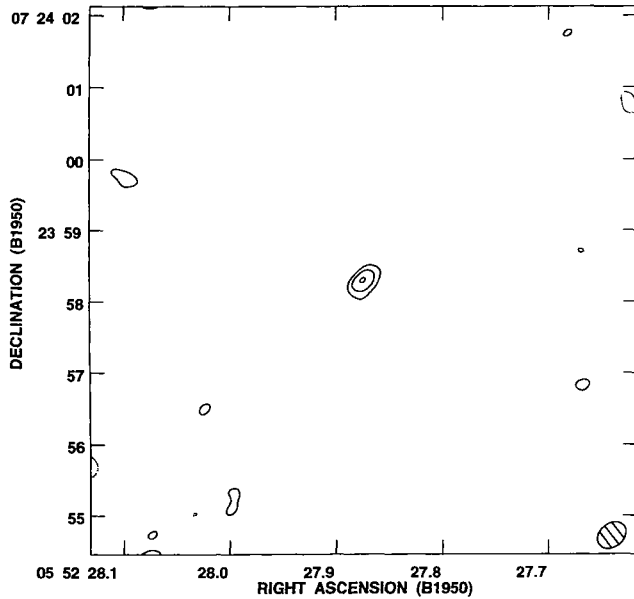


**Figure 1.** 5-GHz MERLIN image of  $\alpha$  Ori. Contour levels are set at  $-3, 3, 4, 5\sigma$  where  $1\sigma$  is  $240 \mu\text{Jy}$ . The data has been tapered with a  $500\text{-k}\lambda$  taper. Tapering effectively weights the data by  $w(b) = C \exp[-(b/b_0)^2]$ , where  $b$  is the baseline,  $b_0$  is the taper and  $C$  is a scaling constant. The resulting full-width at half-maximum (FWHM) of the beam is  $0.43 \times 0.33 \text{ arcsec}^2$ , and is shown in the lower right-hand corner.

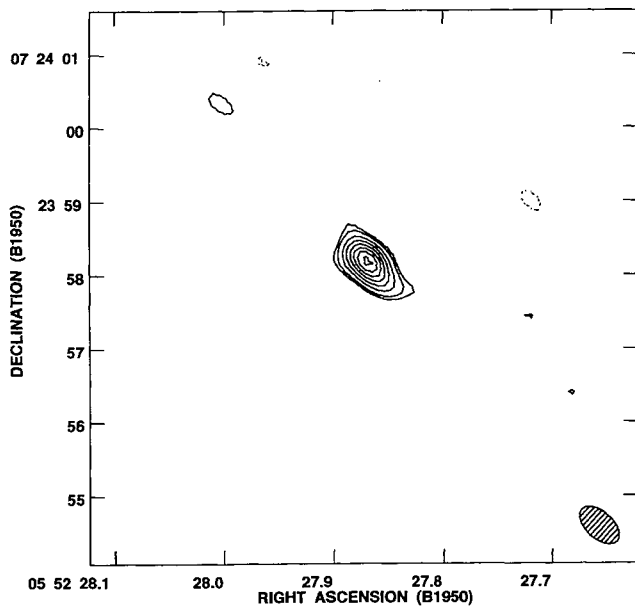


**Figure 2.** VLA 5-GHz image of  $\alpha$  Ori. Contour levels are set to  $-3, 3, 4, 6, 8, 10, 12, 14, 16\sigma$  where  $1\sigma$  is  $74 \mu\text{Jy}$ . The beam FWHM of  $0.65 \times 0.36 \text{ arcsec}^2$  is shown in the lower right-hand corner. No tapering was applied to the visibilities before imaging.

$\alpha$  Ori is resolved in both observations, with a mean source diameter  $\sim 0.36 \text{ arcsec}$ . However, when the source size is so close to that of the telescope beam a more accurate estimate of the source dimensions can be obtained from analysis of the visibility data. An image derived from observations taken with an interferometric array results from Fourier transformation of the 2D complex visibility data that is a function of the baseline coordinates ( $u, v$ ) of the array. At any instant, each baseline pair in the array determines the visibility at a single point in the ( $u, v$ ) plane. For an unresolved source i.e. a point source, at the phase centre of an array, the real amplitude of the complex visibility is independent of baseline length, and equal to the total flux density of the source. This is a consequence of the complex visibility data being a 2D Fourier transform of the source brightness distribution. A resolved source will have visibility amplitude that is a function of the baseline length, and the source dimensions can be derived from the visibility distribution.

After phase-centring, the real visibility amplitudes of  $\alpha$  Ori were calculated as a function of baseline length (Fig. 3), where the baseline length is given by  $\sqrt{u^2 + v^2}$ . The data points in this figure are the means and errors of the real visibility amplitudes within 15 equal-width baseline-distance annuli. The increasing uncertainty with baseline distance is the result of a decreasing number of ( $u, v$ ) points at longer baselines. Fig. 3 clearly shows that over a baseline range of  $\sim 0.5 \text{ M}\lambda$  at 5 GHz the visibility amplitude of the data from both MERLIN and the VLA decreases by  $\sim 80$  per cent, indicating that the emission is well resolved by both MERLIN and the VLA. Indeed,  $\alpha$  Ori is largely resolved out on MERLIN baselines. The dashed line in Fig. 3 represents a circular Gaussian fit to the combined data (see figure caption). The fit parameters for this and similar fits to the individual MERLIN and VLA observations are summarized in Table 1.

It is possible to obtain a decrease in the real amplitude of the visibility data with baseline length because of de-correlation of the antenna-based phases, particularly on longer

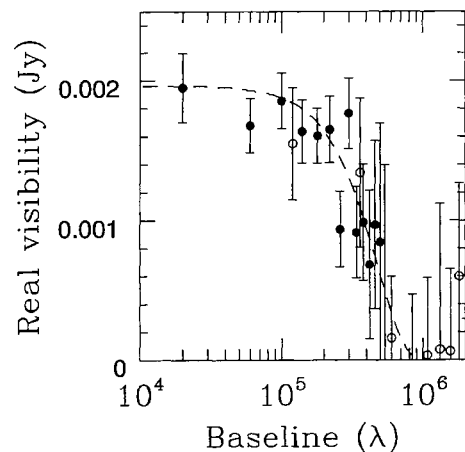


**Figure 3.** The real visibility amplitude of  $\alpha$  Ori from MERLIN (open circles) and VLA (solid circles) observations, as a function of baseline length, in units of wavelengths ( $\lambda$ ). The dashed line represents the best fit to the combined visibilities, using a circular Gaussian source with a FWHM of  $0.222 \text{ arcsec}$ .

**Table 1.** Circular Gaussian fits to the visibility data.

Source	Flux <sup>1</sup>	Visib. FWHM <sup>2</sup> (Mλ)	Image FWHM <sup>3</sup> (mas)	Array
0552+032	0.585 ± 0.001 Jy	23.5 ± 0.26	7.7 ± 0.1	M
0529+075	1.736 ± 0.001	15.6 ± 3.4	12 ± 3	V
α Ori	1.74 ± 0.45 mJy	0.79 ± 0.26	231 ± 77	M
	1.83 ± 0.11	0.84 ± 0.13	217 ± 35	V
	1.84 ± 0.11	0.82 ± 0.12	222 ± 31	C <sup>4</sup>

<sup>1</sup>The zero-spacing flux, equivalent to the total flux of the source.<sup>2</sup>The visibility FWHM from the fitting procedure. The uncertainty is the formal error of the fit.<sup>3</sup>Image FWHM, converted from visibility FWHM using  $H[\text{arcsec}] \phi[\text{M}\lambda] = 0.182$ . M=MERLIN; V=VLA; C=combined MERLIN/VLA.<sup>4</sup>Derived from a fit to visibilities within 1 Mλ of the (*u*, *v*) origin.

baselines, largely because of atmospheric fluctuations. However, this effect, similar to the seeing owing to the atmosphere for optical telescopes, is variable, depending both on the size (i.e. baseline length) of the telescope system and on the stability of the atmosphere when the observations were made. It is highly improbable that decorrelation would occur by chance with the same baseline dependence for the same source with two such different sites and telescopes as MERLIN and the VLA. The fact that both the MERLIN and VLA data show that α Ori is resolved, with the same baseline dependence, *independently* of each other, demonstrates that the decrease in visibility amplitude is an effect owing to the observed radio source, and not arising from decorrelation or calibration effects, and thus that α Ori is resolved by both telescopes at 5 GHz.

### 3 IR IMAGES

Images of α Ori were obtained in the mid-IR using the Berkeley/Livermore Mid-IR Camera (aka Berkcam, Arens et al. 1987; Keto et al. 1992) at the 3.8-m UKIRT on 1991 November 15 and 1992 December 8.

In 1991 images were obtained at wavelengths of 8.2 (shortward of the broad 9.7-μm silicate feature), 9.7 and 12.5 μm (the latter two contaminated by silicate emission: e.g. Skinner & Whitmore 1987), using a circular variable filter with a spectral resolving power of approximately 10. Standard nodding and chopping procedures were used, as described by Ball et al. (1992), in order to remove the large thermal background emission and flat-field the images. The star α CMa (Sirius) was used as a flux calibrator and to measure the point spread function (PSF) at each wavelength. α CMa was taken to have fluxes of 184 and 107 Jy at wavelengths of 0.865 and 11.5 μm respectively, and to have an effective temperature of 9200 K. All images, and one of the α CMa images, are displayed in Fig. 4. A cross pattern is visible in the images in Fig. 4. This is a telescope diffraction pattern, which is present in the source and PSF images at low levels (a few per cent of the peak).

The 1992 images were taken only four days after the MERLIN image, and were taken at wavelengths of 8.2 and 9.7 μm. Once again calibration images of Sirius were obtained, although at 8.2 μm an image of α Tau was also obtained and used as a calibrator. The two images of α Ori are presented in Fig. 5. Again the telescope diffraction pattern is present at low levels. As with the 1991 data, this is most prominent in the 8.2-μm images, but present in the 9.7-μm image as well.

The spatial resolution of all the images, as determined from the FWHM of the Sirius data, was about 1.2–1.4 arcsec. At 8.2 μm the dusty wind is marginally resolved, while at 9.7 and 12.5 μm the wind is more clearly resolved (this is better seen in Figs 6 and 7). These results are superficially similar to those of Sloan, Grasdalen & LeVan (1993), although of significantly higher signal-to-noise ratio. We do not observe a ring of emission at a radius of about 1.6 arcsec as reported by Sloan et al.; neither did Danchi et al. (1992). We suspect this reported ring of emission to be an artefact generated by deconvolution of low signal-to-noise ratio data. In 1991 the dust shell exhibited a flare-like extension to the north-east, which is not present in any of the calibrator images or images of any other source observed on the same night, as well as being generally extended at all position angles. This ‘flare’ is most prominent in the 9.7 and 12.5-μm images, where it appears at surface brightnesses significantly less than 10 per cent of the peak, and extends up to about 3–4 arcsec from the star. In 1992 the images are more symmetric, and appear a little less extended. Azimuthally averaged 1D surface-brightness profiles have been generated from these images, and are displayed in Figs 6 and 7.

### 4 A SELF-CONSISTENT MODEL FOR THE CIRCUMSTELLAR ENVIRONMENT OF α ORI

We have generated a computer program to model our observations of α Ori. The basic elements of the model are the same as those of the model by SW87, but they have been treated in much more detail in order to accommodate the spatial information which we have reported here, and which did not exist in 1987. Departing from SW87, we now generate oversampled images and visibility curves at various wavelengths, as well as the model SED. There are three physical elements to the model.

First, the central star is treated as a blackbody. The basic parameters of the star are its distance, radius and effective temperature. As discussed by SW87, the distance to α Ori is most probably 200 pc. The radius and effective temperature were initially taken to be  $6.4 \times 10^{13}$  cm and 3600 K as determined by SW87, and were then adjusted as necessary in order to provide the best model fit.

SW87 treated the chromosphere very simply, using a 1D approach. At that time this was reasonable, as no spatial information was available on the chromosphere. We have considerably improved upon this by making the model two dimensional. For now we assume the structure to be spherically symmetric (we will discuss this assumption in the following section). The emission is calculated in annuli centred on the disc centre, with impact parameters logarithmically



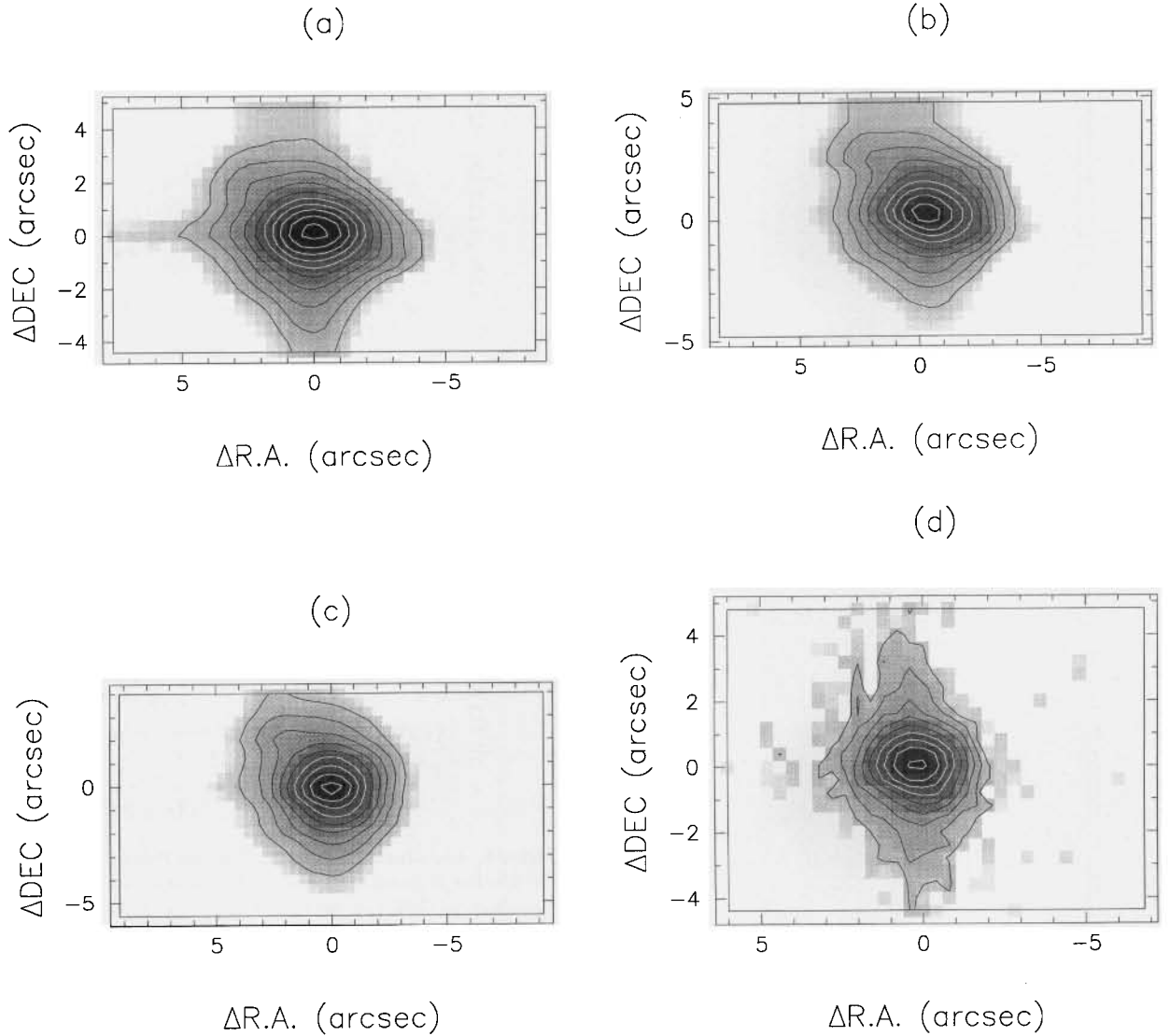


**Figure 4.** Mid-IR images acquired at UKIRT in 1991 November. Contours are logarithmically spaced by 0.23 dex from the peak, and the grey-scale is also logarithmically scaled. (a)  $\alpha$  Ori at  $8.2\ \mu\text{m}$ , peak contour level  $1000\ \text{Jy arcsec}^{-2}$ , (b)  $\alpha$  Ori at  $9.7\ \mu\text{m}$ , peak contour  $1585\ \text{Jy arcsec}^{-2}$ , (c)  $\alpha$  Ori at  $12.5\ \mu\text{m}$ , peak contour  $1000\ \text{Jy arcsec}^{-2}$ , (d)  $\alpha$  CMa, our point-source calibrator, at  $8.2\ \mu\text{m}$ , peak contour  $112\ \text{Jy arcsec}^{-2}$ .

spaced. The volume emissivity of the chromospheric plasma at frequency  $\nu$  in  $\text{erg cm}^{-3}\ \text{s}^{-1}\ \text{Hz}^{-1}$  is

$$\varepsilon(\nu) = 6.8 \times 10^{38} g(\nu, T) n_e^2 e^{-43.2\nu/T_e} T_e^{-0.5} \quad (1)$$

where  $n_e$  is the electron density in  $\text{cm}^{-3}$ ,  $\nu$  is the frequency in GHz,  $T_e$  is the electron temperature in K, and  $g(\nu, T)$  is the Gaunt factor. Assuming local thermodynamic equilibrium (LTE) the optical depth is given by

$$\tau(\nu) = \int \frac{\varepsilon(\nu) l}{B_\nu(\lambda, T_e)} d\lambda \quad (2)$$

where  $B_\nu$  is the Planck function in  $\text{erg cm}^{-2}\ \text{Hz}^{-1}$ , and  $l$  is the path-length along the annulus.

Determination of the Gaunt factor is an important, and non-trivial task. Very few references exist that indicate exactly how to determine these, even approximately. We outline in the Appendix to this paper how the Gaunt factor

for free-free emission may be calculated for emission and absorption in a relatively low-temperature medium such as this. Using these equations, we can now integrate the free-free emission along each annulus. The annular contributions are summed, and so the emergent free-free continuum as a function of wavelength is determined.

The third element is the dust shell. It is treated geometrically in the same manner as the chromosphere, as a set of concentric annuli with logarithmically increasing radii. The inner and outer radii of the dust shell are left as free parameters to be determined by the model fit. The volume emissivity of the dust shell is dependent on the mass-loss rate, the wind velocity, the optical properties of the dust material, and the dust grain temperature. All the relevant equations are described by SW87, and the only difference in this analysis is that we calculate the emission from concentric annuli rather than from the entire dust shell. Again, the geometry of the entire system is assumed to be spherical. Departing

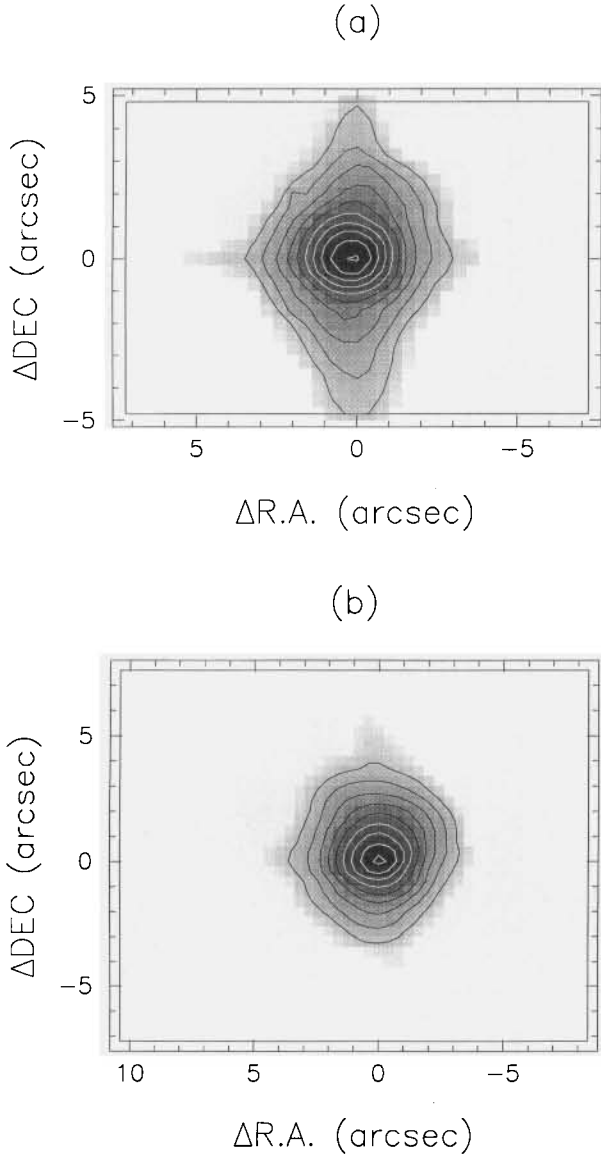


**Figure 5.** Mid-IR images acquired at UKIRT in 1992 December. Contour levels are all spaced logarithmically by 0.23 dex, and the grey-scale is also logarithmically scaled. (a)  $\alpha$  Ori at 8.2  $\mu\text{m}$ , peak contour level 1585  $\text{Jy arcsec}^{-2}$ , (b)  $\alpha$  Ori at 9.7  $\mu\text{m}$ , peak contour 2000  $\text{Jy arcsec}^{-2}$ .

from SW87, we have used the optical constants for silicate dust presented by Draine & Lee (1984). We still use the power-law dust grain size distribution as justified by SW87, namely

$$n_g(r) \propto r^{-\alpha} \quad (3)$$

where  $n_g(r)$  is the relative number of dust grains of radius  $r$ , and  $\alpha$  is a constant, taken to be equal to 3.5 as determined for the ISM (Mathis, Rumpl & Nordsieck 1977).

The resulting model is mapped on to images with 0.1-arcsec pixel size, using a simulated 10 per cent bandpass filter (a rectangular bandpass is assumed, which is close to the spectral response of the camera). A model PSF is also generated, consisting of an elliptical Gaussian core with a circular, power-law halo (this structure provides a good fit

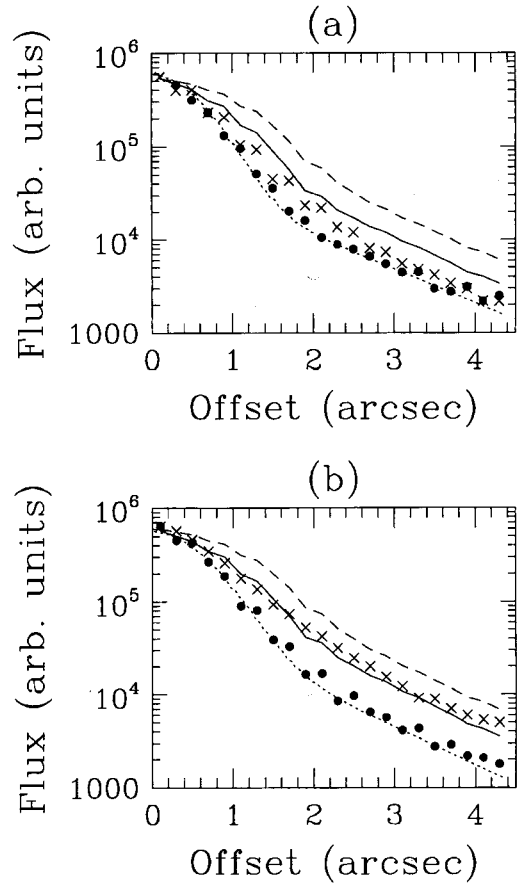


**Figure 6.** The azimuthally averaged model PSF (dotted line) and  $\alpha$  Ori Models A (solid line) and B (dashed line) are compared with our observed (1991) profiles of  $\alpha$  Ori (crosses) and the calibrator  $\alpha$  CMA (filled circles) at (a) 8.2  $\mu\text{m}$  and (b) 9.7  $\mu\text{m}$ .

to the images of  $\alpha$  CMA and  $\alpha$  Tau). The PSF is adjusted to provide a good fit to each of the calibrator images. Now the PSF is convolved with the  $\alpha$  Ori model, and then integrated into larger 0.4-arcsec pixels for comparison with our observed images.

We present in Fig. 8 the electron density and temperature as functions of radius, as determined by our model. The behaviour is qualitatively very similar to those presented by SW87, but the quantities are different. The electron density falls with radius with a roughly inverse-square law, but has a flattening in the 1.03–3.5 photospheric radii region, before dropping much more rapidly. The spatial information provided by our MERLIN and VLA data absolutely require this structure, and the rapid fall in electron density beyond 3.5 photospheric radii is essential in order to simultaneously fit the observed 5-GHz visibility profile and the radio SED. The high temperature in the region with slowly varying electron density is also absolutely required, in order to prevent the free-free optical depth from becoming too large, which would prevent the model from fitting the observed radio SED. The excellent fit of this model to the combined MERLIN plus VLA visibility curve is shown in Fig. 9. (The curve lies a little above most of the points in the visibility curve: this is forced by the model requirement to fit many radio observations at other frequencies. The model none

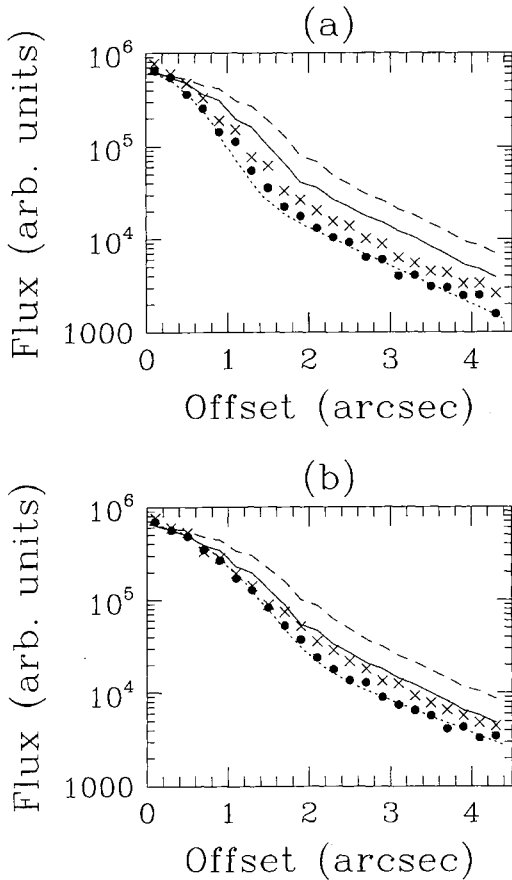


**Figure 7.** The azimuthally averaged model PSF (dotted line) and  $\alpha$  Ori Models A (solid line) and B (dashed line) are compared with our observed (1992) profiles of  $\alpha$  Ori (crosses) and the calibrator (filled circles) at (a)  $8.2\ \mu\text{m}$  (calibrator  $\alpha$  Tau) and (b)  $9.7\ \mu\text{m}$  (calibrator  $\alpha$  CMa).

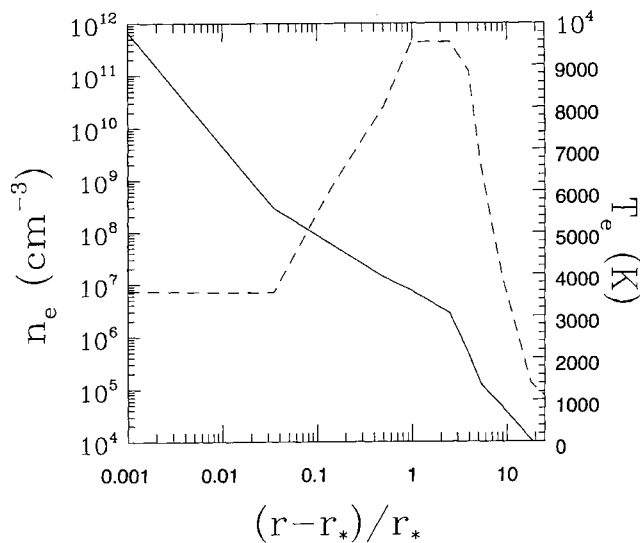


**Figure 8.** Model chromosphere for  $\alpha$  Ori. The value of  $r_*$  (used to define the abscissa) is the photospheric radius. We show the electron density (solid line), and electron temperature (dashed line) as functions of radius.

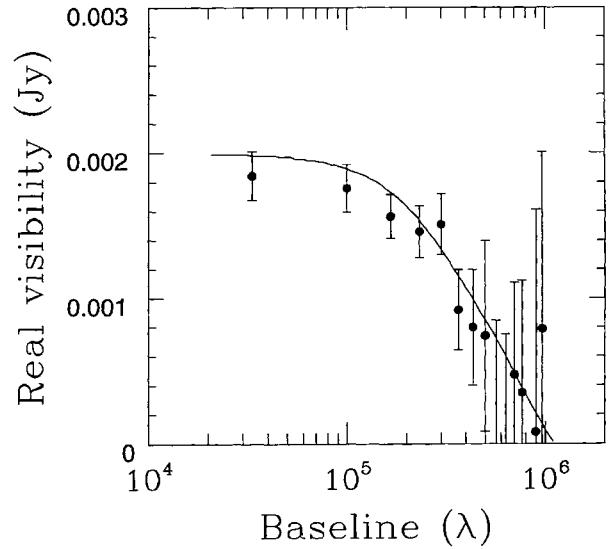


**Figure 9.** Model visibility curve, generated using the model chromosphere depicted in Fig. 8 (solid line). The data are the combined MERLIN plus VLA visibility curve, plotted as solid circles with error bars.

the less passes through the error bars of all the MERLIN data.) In contrast to SW87, we find that free-free emission cannot contribute to the mid-IR excess of  $\alpha$  Ori. Instead the free-free continuum contributes only in the mm and radio wavelength regions. This difference arises partly because of the new spatial constraints we can use for the radio emission, and partly because we now calculate the Gaunt factors as described in the Appendix, whereas SW87 used an approximation which is valid for absorption but not for emission in the mid-IR wavelength region.

In the absence of free-free continuum to flatten the SED in the mid-IR, it is necessary to reduce the temperature of the dust compared to that determined by SW87. The SED of the dust shell is dominated by the warmest grains at the inner edge of the shell, which emit far more energy than the cooler grains further out. By reducing the temperature of the warmest grains, we decrease the gradient of the dust shell spectrum in the mid-IR. As discussed by SW87, the expected condensation temperature of silicate grains in a cool star dust shell is around 1000 K, which in the case of  $\alpha$  Ori would be at about 10 photospheric radii. By increasing the inner radius of the dust shell to about 20 photospheric radii, we are able to flatten the dust shell SED sufficiently to obtain a reasonable fit to the mid-IR spectrum (Fig. 10). This corresponds to an angular radius of about 0.5 arcsec for the inner edge of the dust shell, with our assumed distance to  $\alpha$  Ori of 200 pc. A variety of observations (mostly interferometric) have suggested an inner edge radius of about 0.9–1.0 arcsec (e.g. Sutton et al. 1977; Bloemhof et al. 1984; Dyck & Benson 1992; Danchi et al. 1994). We have run the model using a 0.9-arcsec inner radius for the dust-shell, and we show the resulting fit in Fig. 10. We will henceforth refer to this model as Model B, and to our preferred model, described earlier, as Model A. We find that while the fit of Model B to the 20- $\mu\text{m}$  region of the LRS spectrum is marginally better than that of Model A, it generates a 9.7- $\mu\text{m}$  feature that is far too weak. Among all

the laboratory measurements for silicates, we have found none with a 9.7- $\mu\text{m}$  feature as strong as would be needed to account for the observed feature in  $\alpha$  Ori using Model B. The fit of the two models to the overall SED is shown in Fig. 11. Model B provides rather too much flux at 60 and 100  $\mu\text{m}$  compared with the *IRAS* data. In Figs 6 and 7 we show the fit of both models to the azimuthally averaged 1D profiles of the observations at 8.2 and 9.7  $\mu\text{m}$  from both years. (The fit of Model A to the 1991 12.5- $\mu\text{m}$  data is as good as the fit to the 9.7- $\mu\text{m}$  data, and so is not shown here.) We present the derived model parameters for Model A in Table 2, as well as those others that are needed for the calculations and are taken from sources referred to by SW87.

## 5 DISCUSSION

The results of this work contain some significant differences from those of SW87, and it is therefore natural to question the uniqueness of the model. It is important to bear in mind at the outset that in 1987 there were few spatial constraints available on either the chromosphere or the dust shell of  $\alpha$  Ori. We now have both, and this applies strong constraints to models which can fit the available data. Additionally, we have made numerous improvements to the model of SW87 (many of which are facilitated by the enormous increase in computer speed in the intervening 10 years), which have a significant effect on the model results. We consider here the uniqueness of various aspects of the model.

Our chromospheric model must now fit simultaneously the visibility profiles from the VLA and MERLIN and the observed SED at mm and radio wavelengths. Our radio images show that the chromosphere is larger at these wavelengths than assumed by SW87 (of order 4 photospheric radii, compared with SW87's assumed size of order 2 photospheric radii which was based on some indirect observa-

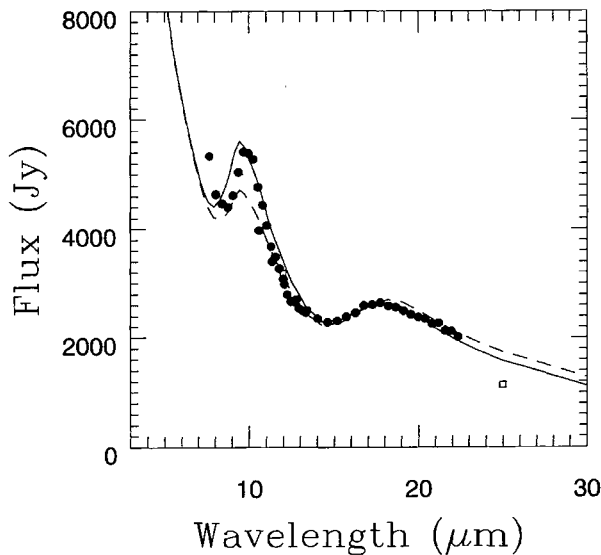


**Figure 10.** The *IRAS* LRS spectrum, recalibrated as recommended by Cohen, Walker & Witteborn (1992), is shown (filled circles), plus colour-corrected *IRAS* Point Source Catalog fluxes (open circles) compared to the results of Model A (solid line) and Model B (dashed line). Model B produces far too weak a 9.7- $\mu\text{m}$  feature.

tional evidence). This has a very strong effect on the model, since the slope of the SED at long wavelengths is determined by the wavelength at which the free-free continuum from a given parcel of gas becomes optically thick, which in turn is determined by the size and electron density of the chromosphere, as well as by its temperature. There is only one model that can acceptably fit both the SED and the visibility curve. We find that adjusting the electron density by a factor of a few over most of the chromosphere causes the fit to the data to deteriorate significantly. Similarly the high temperature is absolutely required in the inner few photospheric radii, and decreasing the temperature here below about 6000 K renders the fit unacceptably poor. We are unable to find any combination of density and temperature that yields an acceptable fit to both the SED and the visibility curve, other than the one presented here. Our

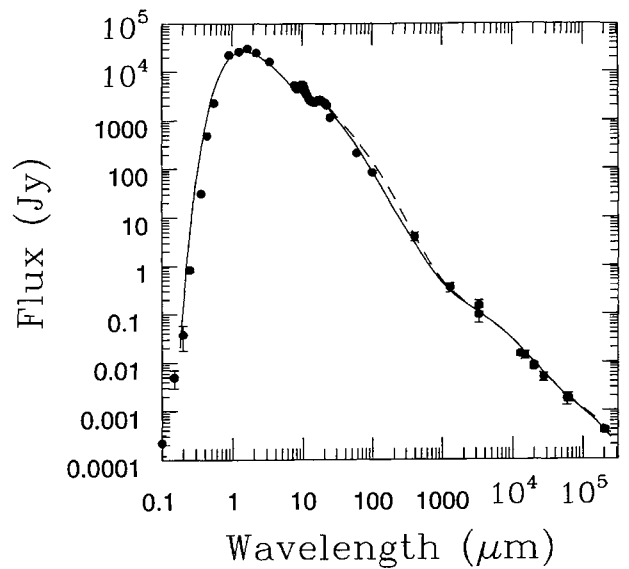


**Figure 11.** The overall SED of  $\alpha$  Ori is shown (filled circles) compared to the results of Model A (solid line) and Model B (dashed line). Model B is seen to produce a slightly better fit to the 400- $\mu\text{m}$  flux, but a poorer fit to the *IRAS* 60- and 100- $\mu\text{m}$  observations. However, the difference is rather small given the uncertainties in the observations.

**Table 2.** Results from Model A.

Stellar radius	$6.5 \times 10^{13}$ cm
Stellar effective temperature	3450K
Distance to star	200pc*
Dust shell inner radius	$1.65 \times 10^{15}$ cm
Dust shell outer radius	$5 \times 10^{18}$ cm
Total Mass-loss Rate	$1.5 \times 10^{-6} M_{\odot}/\text{yr}^*$
Wind velocity	15km/sec*
Dust-to-gas ratio	$2.5 \times 10^{-3}$

\*From SW87.



model fits all of the long-wavelength (mm and longer) observations of  $\alpha$  Ori in its ‘normal’ (i.e. non-flaring) state. Finally, we note that the diameter of the emitting region of the chromosphere of  $\alpha$  Ori as observed with the *HST* at UV wavelengths by Gilliland & Dupree (1996) is a little over 0.1 arcsec, which corresponds very closely to the radius at which the electron temperature begins to drop rapidly in our model. Our 5-GHz images are dominated by material at a similar range of distances from the star, indicating that our model is probably consistent with the *HST* data (Gilliland & Dupree 1996) also. It is to be hoped that the analysis of the emitting region observed with the *HST* can provide estimates of electron density and temperature, which may be compared with ours. Finally, we note that the model for the gas temperature as a function of distance from the star which was adopted by Rodgers & Glassgold (1991) is virtually identical to the distribution determined here, and provided a reasonable fit to the strengths of the O I and Si II far-IR lines observed by Haas & Glassgold (1993), providing further independent support for our model.

There are a number of important caveats to be borne in mind when considering our chromospheric model. First, we have assumed spherical symmetry throughout the model calculations. The visibility data from both MERLIN and the VLA are of a too low a signal-to-noise ratio, and inadequately sample the Fourier plane, to establish whether the chromosphere of  $\alpha$  Ori in fact departs significantly from spherical symmetry. However, there are a number of indications that it almost certainly does. First, the high spatial resolution optical images of Wilson et al. (1992) show clearly that the surface of  $\alpha$  Ori bears large hotspots, which most probably will relate to local asymmetries in the overlying chromosphere. Secondly, speckle images in the H $\alpha$  line revealed a very extended and asymmetric chromosphere around the star (Hebden et al. 1987). Most recently *HST* observations of  $\alpha$  Ori in the near-UV using the Faint Object Camera have been reported (Gilliland & Dupree 1996), showing again that the star has a very large and asymmetric chromosphere. It is unlikely that this asymmetry will make very large changes to any of the numbers we derive from our model, but it will probably have some relatively small effect.

Secondly, our model assumes the chromosphere to be homogeneous. It is quite possible, however, that it may be clumped on some size scale, and this would also have an effect on the model. A highly clumped medium would allow the chromosphere to have somewhat higher electron density in the clumps without significantly affecting the resulting SED or visibility curve. The size of the chromosphere cannot be significantly varied, however, without a deleterious effect on the visibility curve. Thus the model will not be affected by local departures from the homogeneous properties we have derived, provided these irregularities are on a relatively small scale.

Finally, the outer extent of the chromosphere does have a significant effect on the model. We assume the chromosphere to terminate at the inner edge of the dust shell. This is primarily a convenience for modelling purposes. We note that as the outer boundary of the model chromosphere is moved inward or outward by a few stellar radii, the total 5-GHz flux varies by about 0.1 mJy, and the slope of the long-wavelength SED is slightly decreased. This occurs

because as the outer boundary is increased, the volume of low-density, optically thin plasma is increased, and this makes a small, but noticeable, contribution to the radio flux. We are able to use this to place an upper limit of about 40 photospheric radii on the radius of the ionized region – beyond this the electron density or temperature must be negligible.

A variety of earlier observations suggest that  $\alpha$  Ori departs from spherical symmetry. Most prominent are the observations by Wilson et al. (1992), which show that hot-spots appear on the surface of the stellar photosphere, and move on a time-scale of a year. The observations do not show whether the different appearance of the spotted photosphere in images obtained a year apart results from the evolution (i.e. growth and then disappearance) of individual spots, or from their movement across the surface of the star. It is unlikely, however, that stellar rotation causes spots to move across the star, because the rotational period of an M supergiant is likely to be many years.

The profiles plotted in Figs 6 and 7 show that the dust shell has changed its apparent size or brightness during the 1-yr interval between our mid-IR observing runs. In 1991, the fit of our model to the 9.7- $\mu$ m image is quite good, just falling marginally below the observed profile at large radial offset, while in 1992 our model generates a little too much flux at all radial offsets at 9.7  $\mu$ m. At 8.2  $\mu$ m, the model lies slightly above the data for 1991, but lies considerably above the data for 1992. These images suggest that the dust shell appeared slightly larger in 1991 than in 1992. The ‘flare’ to the north-east in the 1991 images is only partly responsible for this difference. This could mean either that the dust shell was warmer at all (or most) radii in 1991 than in 1992, and thus brighter and so exhibiting greater contrast against the stellar PSF, or that the dust shell was actually physically larger at the earlier epoch. The outflow velocity from  $\alpha$  Ori is 15 km s<sup>-1</sup>, which corresponds to about 0.016 arcsec yr<sup>-1</sup> at a distance of 200 pc. Changes in appearance of the dust shell on a 1-yr time-scale therefore cannot be a result of changes in the mass-loss rate or ejection of shells or blobs, since the time-scale for such effects to significantly affect the appearance of the dust shell is a few decades. Therefore we conclude that the dust shell temperature must have been generally higher in 1991 than in 1992. This could arise because the stellar surface temperature was generally higher in 1991, or because the star was larger and therefore more luminous in 1991 (M supergiants are believed to pulsate, varying in surface effective temperature, radius and luminosity as they do so). Photometry by Krisciunas (1992, 1994) shows that while in 1991 November  $\alpha$  Ori had an apparent visual magnitude of 0.36, close to its maximum, during 1992 December it was undergoing a rapid decline in visual magnitude reported by Guinan, Deeney & Miller (1993), and had a visual magnitude of approximately 0.65. This significant decline in visual magnitude is consistent with the decline in apparent brightness of the dust shell between the two dates, but whether the magnitude of the change in dust shell brightness can be explained is not clear.

$\alpha$  Ori has a substantial excess UV flux (relative to a black-body with the photospheric temperature), which can be seen in Fig. 11, and is due to its chromosphere. The extension and asymmetry seen in the recent *HST* images of the

chromosphere of  $\alpha$  Ori (Gilliland & Dupree 1996) suggest that if UV radiation makes a significant contribution to the heating of its dust shell, then the dust shell should have an asymmetric and variable appearance. The strong extension seen to the north-east in our 1991 image may be explained by a bright spot (or collection of spots or active region) facing in this direction that was strongly illuminating the dust shell, leading to an elevated grain temperature in this direction. In order to determine the temperature of the dust, we would need to deconvolve our  $\alpha$  Ori images from the strong, extended PSF contribution, and the signal-to-noise ratio of our calibrator images is not high enough to do this. The bright spot responsible for this elevated heating may also be responsible for the brighter than normal visual flux of  $\alpha$  Ori at this epoch. The fainter dust emission and lower visual magnitude in 1992 is then consistent with the disappearance of this spot. A global change in the stellar luminosity, due to pulsation, might also be responsible for the change in overall dust shell brightness, but it is hard to imagine such a pulsation leading to the asymmetric dust illumination seen in 1991. Wilson et al. (1992) find evidence that the star does indeed change its radius (defined using visual visibility curves) with time: between early 1989 and early 1991 the star appeared to change the radius of its optical photosphere by about 10 per cent. For a constant effective temperature, this would give a change of about 20 per cent in visual brightness. From the data presented by Krisciunas (1992), over the same period the star changed its visual brightness by about 50 per cent. Assuming that the estimated uncertainties in angular diameter determination by Wilson et al. are reasonable, this requires an *increase* in stellar effective temperature as the star increases its radius, or an additional mechanism to provide visual flux variations. Spots on the stellar surface may provide the additional mechanism. Wilson et al. estimate that a single spot may provide as much as 10 per cent of the total visual flux. The brightness maximum in late 1991 may have represented a period of unusual activity for the star, in which case one might suppose that as much as 20 per cent of the total visual flux might arise in hotspots.

The size of the ‘flare’ to the north-east of the star in our 1991 data is surprising. It extends over three to four arcsec, which is of order  $10^{16}$  cm at 200 pc. For a ‘typical’ interstellar grain size distribution (Mathis et al. 1977) as adopted in our models, at this distance from the star the equilibrium temperature for grains is in the range 180–250 K, a temperature at which we would not expect them to emit substantially at wavelengths as short as 8  $\mu$ m. Since the *HST* images imply that the chromosphere of  $\alpha$  Ori may be asymmetric, and as we have speculated that its structure and UV flux may be time variable, it is possible that at some times the UV flux from the chromosphere may lead some fraction of the population of small grains in the dust shell of  $\alpha$  Ori to be at higher than equilibrium temperature, via the well-known single-photon small-grain-heating process. An effective grain temperature elevation of less than 100 K would suffice to explain the extended ‘flare’ in our 1991 data. Such a mechanism could be tested only by monitoring  $\alpha$  Ori simultaneously in the radio, the mid-IR and the UV. The radio data would provide information on any chromospheric activity, the mid-IR would investigate the effect of chromospheric activity on the dust shell, and the UV (*HST*) obser-

vations would confirm that asymmetries in the mid-IR result from asymmetries in the illuminating radiation field.

If the dust shell and chromosphere spatially overlapped, then the UV radiation which is evident in Fig. 11 would surround the dust grains at the inner edge of the dust shell. This could lead to significant extra heating of the grains. However, the *HST* images, as well as the ground-based optical images in H $\alpha$ , suggest that the majority of the UV line radiation probably arises within a few photospheric radii of the star, an order of magnitude smaller than the dust shell inner radius. Inspection of Fig. 11 reveals that the total chromospheric UV flux is so much smaller than the optical photospheric flux that it is unlikely to significantly affect the grain temperatures (except possibly for any very small grains, as mentioned above).

How consistent are our dust shell results with previous observations? Asymmetry in observations of the circumstellar envelope of  $\alpha$  Ori has been reported before. Bloemhof et al. (1984) reported considerable east–west asymmetry in the dust shell of  $\alpha$  Ori, with the brightest emission to the west. This is just the opposite of what we have found, emphasizing the likely morphological variability for this star. However, it is worth pointing out that their PSF calibrator,  $\alpha$  Boo, also seems to show some east–west asymmetry in the same sense. It is noteworthy also that Bloemhof, Danchi & Townes (1985) reported a change in the brightness of the dust shell on a 1-yr time-scale, similar to the phenomenon we report here.

Previous determinations of the dust shell inner radius have included Danchi et al. (1994; 1.0 arcsec from Michelson interferometry at 11  $\mu$ m), Sloan et al. (1993; 0.5–1 arcsec from 8–13  $\mu$ m spectral images), Dyck & Benson (1992; 1.3 arcsec from 11- $\mu$ m speckle interferometry), Benson, Turner & Dyck (1989; 1.4 arcsec from *N*-band speckle interferometry), Bloemhof et al. (1984; 0.9 arcsec from diffraction-limited spatial scans at 9.3  $\mu$ m), and Sutton et al. (1977; > 0.7 arcsec from Michelson interferometry at 11.1  $\mu$ m). All of these studies conclude that the size of the dust shell inner radius is larger (typically by about a factor of 2) than we have found. These differences are difficult to resolve. In the case of the observations by Bloemhof et al. (1984, 1985), the inferred dust shell diameter resulted from data where the PSF had not been deconvolved. Our models indicate that indeed the difference between the PSF and the dust shell observation should only become large and easily visible to the eye on a linear scale at radii close to 1 arcsec, consistent with the data of Bloemhof et al. The data of Sloan et al. had rather large pixel size and very low signal-to-noise ratio, and were both interpolated spatially and then deconvolved in order to estimate an inner radius for the dust shell, and so it is hard to estimate how reliable such a determination can be. Our models also demonstrate that a dust shell inner radius as large as 1 arcsec is quite inconsistent with our images. Defective optics or poor focus could certainly make a source appear larger than it should in a simple array camera such as the Berkeley Camera, but it is indeed difficult to make a source appear *smaller* than it should. The alternative explanation, that the source is really much smaller than the interferometric observations imply, is also difficult to accept because of the large number of observations which have reached similar conclusions concerning the large size of the  $\alpha$  Ori dust shell. We show in Fig.

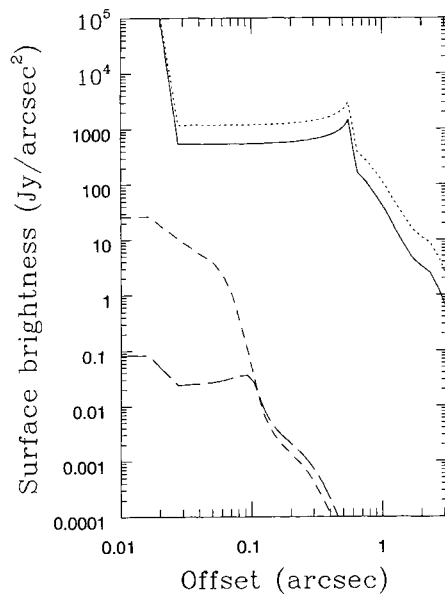


**Figure 12.** Intrinsic radial profiles generated by our Model A at wavelengths of 8.2  $\mu\text{m}$  (solid line), 12.5  $\mu\text{m}$  (dotted line), 3.3 mm (short-dashed line) and 6 cm (long-dashed line).

12 the intrinsic radial profiles generated by our model at mid-IR and radio wavelengths. The radiative transfer models of Rowan-Robinson et al. (1986) obtained an inner dust shell radius of 0.78 arcsec, intermediate between our model and the interferometer results. Rowan-Robinson et al. used a ‘modified dirty silicate’ dust, which has higher absorption than our Draine & Lee grains at short wavelengths, allowing their dust shell to have a similar temperature, and thus SED, to ours at its inner radius. Whilst this would allow our model a better fit to the size measured by the spatial interferometric techniques, it would still be inconsistent with our direct images. We are therefore left with the conundrum that spatial interferometer observations are consistently providing results which are inconsistent with radiative transfer models (using unmodified grain data) and our direct imaging results. We now note that the only high-quality direct image of  $\alpha$  Ori at mid-IR wavelengths that has previously been published is that of Danchi et al. (1992). Their PSF-subtracted image very clearly shows a ring of dust emission with a radius of approximately 0.6 arcsec, very close to the inner radius we derive. Inexplicably, Danchi et al. state that their image is ‘clearly showing an approximately 1 arcsec inner radius’, a statement we find quite impossible to resolve with the image for which this is the caption. The analysis of the interferometric results is dependent on roughly circular symmetry in the source. Since we have shown that the dust shell is, at least sometimes, asymmetric, there may be some latitude for misinterpretation of the interferometric observations, but it is not clear whether this can explain the size of the difference between our direct imaging results and those from spatial interferometry.

At both the 1991 and 1992 epochs of our mid-IR images, our model slightly overestimates the extension of the dust shell at 8.2  $\mu\text{m}$ . As can be seen in Fig. 10, the 9.7- $\mu\text{m}$  silicate feature produced by our model is somewhat too broad on the short-wavelength side, and this is probably responsible

for the ‘excess’ extension seen in the radial profiles. Figs 6 and 7 show that making the dust shell larger does not cure this problem, but actually exacerbates it, because the size of the PSF is comparable with the inner radius of the dust shell and the dust shell flux is comparable with the stellar flux.

The dust-to-gas ratio quoted in Table 2 is obtained by comparing our dust mass-loss rate with the 21-cm H I result of Bowers & Knapp (1987). The typical interstellar value is believed to be of order 0.01 (e.g. Mathis et al. 1977), so our value would indicate that the ratio for  $\alpha$  Ori is rather low. We note that if the inner radius of the dust shell is 1 arcsec, then the dust-to-gas ratio becomes  $5 \times 10^{-3}$ , which is much closer to the interstellar value.

## 6 CONCLUSIONS

We have for the first time resolved the chromosphere of  $\alpha$  Ori in the radio, at a wavelength of 6 cm. We have also presented mid-IR images of the star which resolve the dust shell. Mid-IR images taken at different epochs show that the morphology and shell brightness are somewhat variable, consistent with earlier results, and we suggest that this may be due to an asymmetric, time-variable illumination by the central star. This may simply be a reflection of the growth and evolution of hotspots on the surface of the star, which may also influence the morphology of the overlying chromosphere. We have presented a model for the chromosphere and dust shell, which is consistent both with our images in the radio and in the mid-IR, and with the SED of the source. From this model we show that the chromosphere has a typical radius of about four photospheric radii, and a maximum temperature of the order of 9000 K. This model is strongly constrained by the variety of observational data which now exist for this star at radio wavelengths. Our dust shell model, however, implies an inner radius of about 25 photospheric radii, which is almost a factor of 2 smaller than implied by various interferometric size determinations, although it is entirely consistent with our direct images. We are unable to explain this apparent contradiction.

## REFERENCES

- Arens J. F., Jernigan J. G., Ball R., Peck M. C., Gaalema S., Lacy J., 1987, in Wynn-Williams C. G., Becklin E., eds, *Infrared Astronomy with Arrays*. Univ. Hawaii, Honolulu, 256
- Ball R., Arens J. F., Jernigan J. G., Keto E., Meixner M., 1992, *ApJ*, 389, 616
- Benson J. A., Turner N. H., Dyck H. M., 1989, *AJ*, 97, 1763
- Bloemhof E. E., Townes C. H., Vanderwyck A. H. B., 1984, *ApJ*, 276, L21
- Bloemhof E. E., Danchi W. C., Townes C. H., 1985, *ApJ*, 299, L37
- Bowers P. F., Knapp G. R., 1987, *ApJ*, 315, 305
- Brussard P. J., van de Hulst H. C., 1962, *Rev. Mod. Phys.*, 34, 507
- Cohen M., Walker R. G., Witteborn F. C., 1992, *AJ*, 104, 2030
- Danchi W. C., Degiacomi C. G., Bester M., Greenhill L. J., Gezari D. Y., 1992, in Beckers J. M., Merkle F., eds, *High Resolution Imaging by Interferometry II*. ESO, Garching-bei-Munchen, p. 21
- Danchi W. C., Bester M., Degiacomi C. G., Greenhill L. J., Townes C. H., 1994, *AJ*, 107, 1469
- Draine B. T., Lee H. M., 1984, *ApJ*, 285, 89



- Dyck H. M., Benson J. A., 1992, *AJ*, 104, 377  
 Gilliland R. L., Dupree A. K., 1996, *ApJ*, 463, L29  
 Guinan E., Deeney B., Miller K., 1993, *IAU Circ. No.* 5708  
 Haas M. R., Glassgold A. E., 1993, *ApJ*, 410, L111  
 Hebden J. C., Eckart A., Hege E. K., 1987, *ApJ*, 314, 690  
 Keto E., Ball R., Arens J. F., Jernigan J. G., Meixner M., 1992, *Int. J. Infrared Millimeter Waves*, 13, N11:1709  
 Knapp G. R., Morris M., 1985, *ApJ*, 292, 640  
 Knapp G. R., 1985, *ApJ*, 293, 273  
 Krisciunas K., 1992, *Inf. Bull. Variable Stars*, No. 3728  
 Krisciunas K., 1994, *Inf. Bull. Variable Stars*, No. 4028  
 Lang K. R., 1980, *Astrophysical Formulae: a Compendium for the Physicist and Astrophysicist*, 2nd edn. Springer-Verlag, Berlin  
 Mathis J. S., Rimpl W., Nordsieck K. H., 1977, *ApJ*, 217, 425  
 Mauron N., Querci F., 1990, *A&AS*, 86, 513  
 Newell R. T., Hjellming R. M., 1982, *ApJ*, 263, L85  
 Oster L., 1970, *A&A*, 9, 318  
 Rodgers B., Glassgold A. E., 1992, *ApJ*, 382, 606  
 Rowan-Robinson M., Lock T. D., Walker D. W., Harris S., 1986, *MNRAS*, 222, 273  
 Schwarzschild M., 1975, *ApJ*, 195, 137  
 Skinner C. J., Whitmore B., 1987, *MNRAS*, 224, 335  
 Skinner C. J., Whitmore B., 1988, *MNRAS*, 235, 603  
 Sloan G. C., Grasdalen G. L., LeVan P. D., 1993, *ApJ*, 404, 328  
 Sutton E. C., Storey J. W. V., Betz A. L., Townes C. H., Spears D. L., 1977, *ApJ*, 217, L97  
 Sylvester R. J., Barlow M. J., Skinner C. J., 1994, *MNRAS*, 266, 640  
 Wilson R. W., Baldwin J. E., Buscher D. F., Warner P. J., 1992, *MNRAS*, 257, 369

## APPENDIX: GAUNT FACTOR CALCULATION

Lang (1980) gives a useful set of approximate formulae to calculate the Gaunt factors under various conditions, from a logarithm factor  $\Lambda$ . Unfortunately he omits the vital information on how to proceed when the value of  $\Lambda$  falls below unity, under which circumstances the Gaunt factor would become negative using the formulae listed. A discussion of this situation is given by Oster (1970), and we use his prescription to modify the results of Lang. As a result, the Gaunt factor for frequency  $\nu$  and temperature  $T$  is determined as follows.

$$g(\nu, T) = \frac{\sqrt{3}}{\pi} \ln \Lambda. \quad (\text{A1})$$

The plasma frequency is given by

$$\omega_p = 5.64 \times 10^4 \sqrt{n_e} \quad (\text{A2})$$

where  $n_e$  is the electron density. For radian frequencies less than or equal to  $\omega_p$ ,

$$\Lambda \approx 3.1 \times 10^3 \frac{T^{1.5}}{Z \sqrt{n_e}}, \quad (\text{A3})$$

where  $Z$  is the mean charge per ion, while for radian frequencies significantly larger than this,

$$\Lambda \approx 5.0 \times 10^7 \frac{T^{1.5}}{Z \nu}. \quad (\text{A4})$$

An interesting and very important subtlety commented upon by Oster (1970) is that the Gaunt factors for absorption and emission of free-free radiation are not necessarily the same. At a certain frequency, as mentioned above, the Gaunt factor would become negative, following equation (A1). In practice, the Gaunt factor tends asymptotically to a limiting value given by Brussaard & van de Hulst (1962)

$$g(\nu, T) = 1.0 + 0.173|n_1|^{-2/3} - 0.050|n_1|^{-4/3} + \dots \quad (\text{A5})$$

where

$$|n_1| = \frac{2\pi}{10^4} \left( \frac{Z}{h\sqrt{T_e}} \right)^{3/2} e^2 \sqrt{m} \quad (\text{A6})$$

$h$  being the Planck constant,  $e$  the electron charge and  $m$  the electron mass. In most stellar wind sources, this limiting value will be very close to unity. This asymptotic value allows us to determine the Gaunt factor for absorption for all situations. For an electron with a given energy, this is a limiting frequency to the photons it can emit. Since for a given electron temperature the electrons will have a Maxwellian distribution of velocities, again this implies that the efficiency of free-free emission drops asymptotically toward zero for some limiting frequency. The result is that the limit calculated above using the equation of Brussaard & van de Hulst must be modified by a term  $e^{-h\nu/kT_e}$ . At high frequency the Gaunt factor for emission thus becomes very small.